Stable hexagonal ternary alloy phase in Fe-Si-H at 28.6–42.2 GPa and 3000 K

Suyu Fu [1,*] Stella Chariton,[2] Vitali B. Prakapenka,[2] Andrew Chizmeshya,[3] and Sang-Heon Shim [1,*]

[1]*School of Earth and Space Exploration, Arizona State University, Tempe, Arizona, USA*
[2]*Center for Advanced Radiation Sources, University of Chicago, Chicago, Illinois, USA*
[3]*School of Molecular Sciences, Arizona State University, Tempe, Arizona, USA*

(Received 15 September 2021; revised 12 February 2022; accepted 8 March 2022; published 21 March 2022)

Hydrogen (H) and silicon (Si) are considered as important light elements for the planetary cores. A large amount of H is able to alloy with pure Fe metal at high pressures. Si can also alloy well with Fe. However, it remains uncertain how much H can alloy with iron silicides and if it alloys how H can alter the crystal structures of Fe-Si alloys at high pressures-temperatures (P-T). We performed experiments on Fe-9Si and Fe-16Si alloys (9 and 16 wt % Si, respectively) in a H medium up to 42.2 GPa and 3000 K in diamond-anvil cells coupled with pulsed laser heating and gated synchrotron x-ray diffraction techniques. We found conversion of the Fe-Si alloys into Fe-rich (fcc and dhcp FeH_x), Si-rich (B20 and B2 FeSi), and intermediate ($Fe_5Si_3H_x$) phases. The new $Fe_5Si_3H_x$ phase has a structure similar to the hexagonal Fe_5Si_3 phase but with expanded volumes, and thus, possible H incorporation. Both the observed volume expansion and the H content estimated by density-functional theory calculations support a significant amount of H with H/Fe $\approx$ 0.6 in the crystal structure. Because Fe_5Si_3 is known to break down above $\sim$1300 K at $\sim$18 GPa, our results suggest that hydrogen stabilizes the hexagonal structure at high P-T. These results have implications for the crystallization of Fe-rich liquid at the solid-to-liquid boundary of planetary cores and possible existence of chemical heterogeneities in the solid cores.

DOI: 10.1103/PhysRevB.105.104111

I. INTRODUCTION

Light siderophile (Fe-loving) elements partitioned into the core-forming iron metal liquid in the early stage of planets' history. They then play an important role in the subsequent dynamics and evolution of the cores [1,2]. Hydrogen (H) is the most abundant element in the universe and is considered to be one of the possible light elements in Fe-rich planetary cores [3,4]. Although it has been controversial [5–7], recent experimental and theoretical studies suggested that as much as 0.3–0.6 wt % H can be incorporated into Earth's core [8,9]. Furthermore, because of the coexistence of abundant molten Fe and silicate melt during the formation of early planetary cores, a large amount of Si can alloy with Fe metal to form Fe-Si alloys under a reducing condition [10,11]. For instance, some geochemical and geophysical constraints suggest that up to 12 wt % Si can exist in the Earth's core, which would make Si the most abundant light element there. Despite the significance of Fe–Si–H system for planetary cores, the effect of H on Fe–Si alloys under relevant pressure and temperature (P-T) conditions is still limited due to technical challenges involved in studying H in laser-heated diamond anvil cells (LHDACs).

The binary Fe–Si system has multiples of stable phases with different compositions at ambient conditions, such as the orthorhombic $FeSi_2$, tetragonal Fe_3Si_7, hexagonal Fe_5Si_3, and cubic Fe_2Si [12–14]. When H was involved, early studies show that the H content in hcp $Fe_{0.88}Si_{0.12}$ (Fe-6.5Si) is 1.2–1.5 wt % by laser heating below 1000 K at 27 and 62 GPa [15], which is much smaller than that in pure Fe metal, up to 8 wt % H above 130 GPa [16–18]. However, the heating temperature is much lower than what expected for planetary cores. Furthermore, how the H incorporation in Fe-Si alloys would change the high P-T phase relations is still unclear.

In this study, we reacted Fe-Si alloys and H up to 42.2 GPa and 3000 K in LHDACs by using pulsed laser heating combined with gated synchrotron x-ray diffraction (XRD) techniques. Fe-9Si ($Fe_{0.83}Si_{0.17}$) and Fe-16Si ($Fe_{0.72}Si_{0.28}$) (9 wt% and 16 wt% Si, respectively) were studied separately. High-pressure XRD patterns and chemical analyses on the recovered heated spots show that both Fe-9Si and Fe-16Si convert into FeH_x with $x \approx 1$ [face-centered-cubic (fcc) and double hexagonal-close-packed (dhcp)], FeSi (B20 and B2), and a hexagonal-structured $Fe_5Si_3H_x$ (x is close to 3). We conducted complementary density-functional theory (DFT) calculations to estimate the amount of H from the experimentally measured unit-cell volume.

II. EXPERIMENTAL PROCEDURE

Both starting materials (Fe-9Si and Fe-16Si) were obtained as powders with average grain sizes of 3–5 μm from GoodFellow Corporation. Electron probe microanalysis (EPMA) (JEOL JXA-8530F) was conducted on more than ten randomly selected points of each sample (Table S1) [19]. The results show that both alloys are chemically homogeneous with Si contents of 8.84 ± 0.30 wt % (Fe-9Si) and 15.93 ± 0.31 wt % (Fe-16Si). The Si content in Fe-9Si alloy is comparable to those reported in previous

*Corresponding authors: suyufu@asu.edu; shdshim@asu.edu

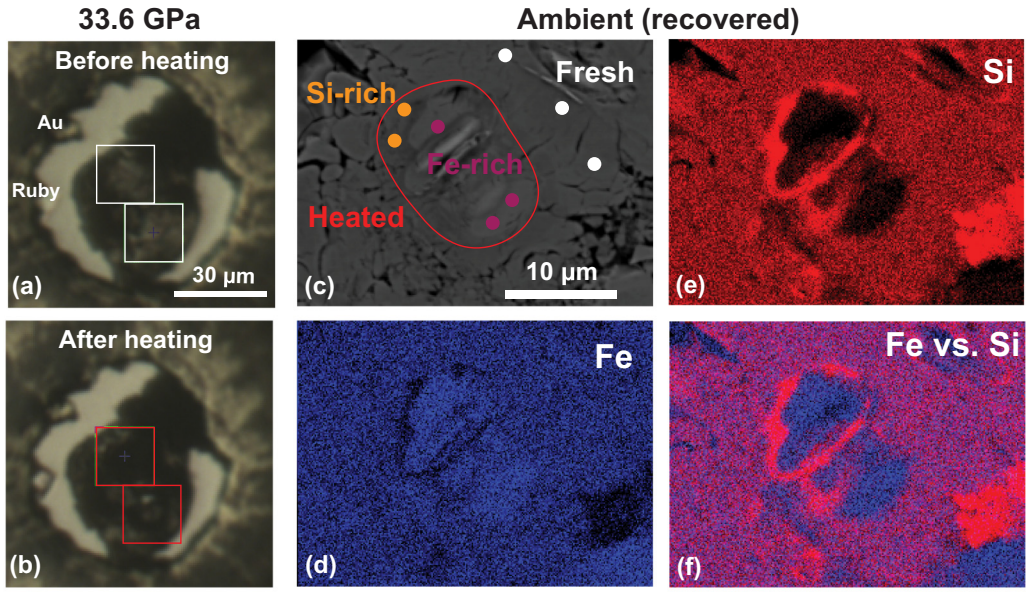

FIG. 1. Optical images of the sample chamber in a diamond anvil cell (a) before and (b) after heating at 33.6 GPa in a Fe-16Si run. The red rectangles in (b) show small transparent spots surrounded by dark areas after heating up to 3000 K, distinct from the flat and smooth surfaces of the fresh sample before heating (white rectangles in (a)). (c)–(f) Electron probe microanalysis on the recovered sample from a Fe-16Si run after high *P-T* reactions with H. (c) Electron back-scattered image of the recovered sample. A heated area is indicated by a red loop, showing a different texture from that of the unheated region. (d) and (e) Energy dispersive spectroscopy mapping of Fe and Si, respectively. (f) Chemical contrast between Fe and Si. The chemical mapping shows that the fresh Fe-16Si is chemically homogeneous, while the heated region has a Si-rich rim with the Si-poor center. Quantitative chemical measurements were conducted on selected points using wavelength-dispersive spectroscopy and they are indicated by dots in (c) with results presented in Table S2 [19].

experiments within uncertainties: 8.62 ± 0.03 wt % [20], 8.7 ± 0.3 wt % [21], 8.75 ± 0.40 wt % [22], and 8.87 ± 0.54 wt % [23]. Both powders were pressed into 5–10-μm thick foils and then separately loaded into DACs for high *P-T* experiments. The sample chambers were prepared by using symmetric DACs with culet sizes of 200 μm. Re gaskets were preindented to 25–30 GPa for $\sim$20 μm thicknesses and 130-μm holes were drilled in the preindented areas to serve as sample chambers. A layer of $>$80-Å thick gold was coated on each side of prepared gaskets to prevent embrittlement by H at high *P-T*. To avoid contact between the loaded sample foils and diamond anvils, foils were propped on both sides by small pieces of the same starting materials. This configuration also provides better thermal insulation and laser coupling during heating. A piece of Au and ruby were placed close to the sample within the chamber to serve as pressure calibrants [24]. Pure H_2 gas was then loaded into DACs as a hydrogen source and pressure medium using a gas loading system at Arizona State University.

High *P-T* experiments were performed by employing pulsed laser heating together with synchrotron XRD at the 13-IDD beamline of the GeoSoilEnviroCARS (GSECARS) sector of the Advanced Photon Source (APS), Argonne National Laboratory (ANL). Two 1064-nm wavelength infrared laser beams at the beamline were focused on both sides of the sample with a flat-top spot size of around 15-μm in diameter [25]. H can diffuse into diamonds and cause them to become brittle at high *P-T*. Therefore, laser heating was carried out in the pulsed mode at a repetition rate of 10 kHz. Because of the high diffusivity of H into metals, $\sim 10^3$ $\mu m^2/s$ even at low *P-T* [26], our experimental setup has shown to allow full reactions between the Fe-Si alloys ($\sim$1 μm grain size at high pressure) and H [27]. The pulsed laser beams were coaxially aligned with an incident monochromatic x-ray beam with a wavelength of 0.3344 Å and a spot size of 3 μm $\times$ 4 μm. The heating temperature was calculated by fitting the collected thermal radiation spectra from both sides of the sample to a Plank function based on a gray-body approximation [Fig. S1] [19].

In the Fe-9Si run, the sample in DAC was compressed to 28.6 GPa and pulsed heating was conducted up to 2610 K. XRD data were then collected during compression on both heated center and unheated region up to 42.2 GPa. Further heating experiments were performed on a new fresh Fe-9Si region to react with H at 42.2 GPa up to 2500 K. In the Fe-16Si run, we directly compressed the sample to 33.6 GPa and heated up to 3000 K [Figs. 1(a)–1(b)]. During decompression, 2D XRD images were collected at the center of heated spots in both Fe-9Si and Fe-16Si runs. Diffraction images were collected using a Pilatus detector. PeakPo software was used for peak identifications [28]. Rietveld refinements were performed on XRD patterns to obtain the unit-cell parameters of synthesized phases using GSAS II [Figs. 2–5] [29]. In this paper, we divided the unit-cell volume of each phase by the number of total Fe and Si atoms in a unit cell, which enables us to directly compare volumes of alloy phases with different compositions. Accordingly, the unit of volume is $Å^3$/(# of Fe+Si atoms). Electron probe microanalyses were conducted on the recovered samples at Eyring Materials Center of Arizona State University in order to determine the

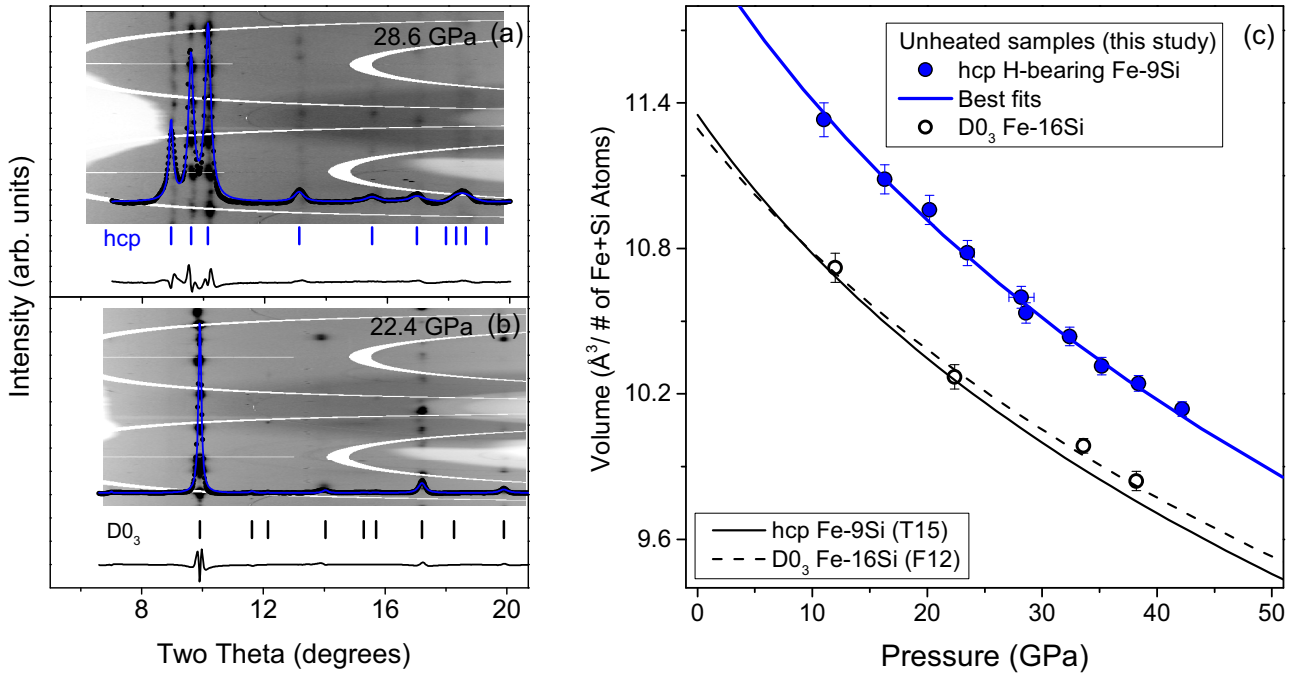

FIG. 2. X-ray diffraction results on cold-compressed, unheated Fe-Si alloys in a H medium at high pressure. (a) Cold-compressed hcp H-bearing Fe-9Si at 28.6 GPa. (b) Cold-compressed $D0_3$ Fe-16Si at 22.4 GPa. (c) Pressure-volume relationship of cold-compressed H-bearing Fe-9Si and Fe-16Si alloys. In (a) and (b), Rietveld refinements were performed to obtain the unit-cell parameters. The black circles are experimental data, the blue lines are the best fits, and the black lines are residuals. The blue and black ticks represent calculated peak positions of the hcp and $D0_3$ phases, respectively. Diffraction images are shown as backgrounds. The wavelength of incident x-ray is 0.3344 Å. In (c), the solid blue and open black circles are cold-compression data of hcp H-bearing Fe-9Si and $D0_3$ Fe-16Si, respectively. EoSs of H-free hcp Fe-9Si (T15) [41] and $D0_3$ Fe-16Si (F12) [42] were plotted as solid and dashed lines, respectively, for comparison. The solid blue line is the best third order BM EoS fit for hcp H bearing Fe-9Si (Table S4) [19]. We did not fit the P-V data of $D0_3$ Fe-16Si because of its agreement with EoS of H-free $D0_3$ Fe-16Si [42].

elemental distribution across the heated region [Figs. 1(c)–1(f)] (Table S2) [19]. The JEOL JXA-8530F electron microprobe operated at an accelerating voltage of 15 eV and a beam current of 20 nA.

III. DENSITY FUNCTION THEORY CALCULATION

Complementary DFT calculations were carried out to estimate the amount of H (x) in the synthesized $Fe_5Si_3H_x$ phase by comparing with our experimental observations. We employed the projector augmented-wave (PAW) method in combination with the Perdew-Burke-Ernzerhof version of generalized gradient approximation (GGA) by using the GPAW package [30–32]. Previous studies on the unit-cell volumes of Fe-Si and Fe-H alloys using GGA have shown agreements with experiments (<1% difference) [33,34]. In the crystal structure of Fe_5Si_3 [35], H can occupy the interstitial sites, surrounded by 4Fe and 2Si at positions of (0.5, 0.5, 0.5), (0.5, 0, 0.5), and (0.5, 0, 0), to form $Fe_5Si_3H_3$. $Fe_5Si_3H_3$ and Fe_5Si_3 have 22 and 16 atoms per unit cell, respectively [Fig. 7(a)]. Electronic and structural convergences were carefully tested for each system. We eventually used a kinetic energy cutoff of 800 eV for Fe_5Si_3 and 900 eV for $Fe_5Si_3H_3$ with Γ-centered k-point grids and a density of 3.5 $Å^{-1}$ or higher, which allows for calculations with a sufficient accuracy and efficiency in this study. We also attempted other possible H locations in Fe_5Si_3 [19]. However, the sites discussed above yielded the best convergence.

In an Fe-Si alloy, magnetic ordering of Fe as well as H can affect its unit cell volume. Accordingly, we considered both nonmagnetic (NM) and ferromagnetic (FM) orderings for H-free and H-bearing phases in the calculation. Early Mössbauer and neutron-diffraction measurements have shown that Fe_5Si_3 is ferromagnetic at 1 bar and has two crystallographically distinct Fe sites with spin directions parallel to the hexagonal c axis, where 4Fe(I) and 6Fe(II) have magnetic moments of 1.05(15) μB and 1.55(15) μB, respectively, at 100–290 K [36]. To understand the impact of magnetic ordering, we initiated the calculation on FM $Fe_5Si_3H_3$ using the same magnetic moments as FM Fe_5Si_3. At each selected volume for a given structure, the external and internal parameters were relaxed by calculating forces on atoms until the maximum total force on all individual atoms is less than 0.005 eV/$Å^3$, except for FM $Fe_5Si_3H_3$ at pressures above 25 GPa where the optimization became challenging. This calculation yields unit-cell parameters which were compared with experimentally observed values. We also conducted several tests on Fe_5Si_3 at 0 GPa by using the DFT + U approach to account for potential electronic interactions in the Supplemental Material [19] (see also Refs. [37,38] therein). We used different values of 1, 2, and 4 eV for the effective U parameter, U_{eff}. However, including U increases the discrepancy in magnetic moments between DFT and experimentally reported values [36]. Therefore, we did not consider the U term in our calculations. Our standard DFT calculations were conducted up to 40 GPa with a 10 GPa

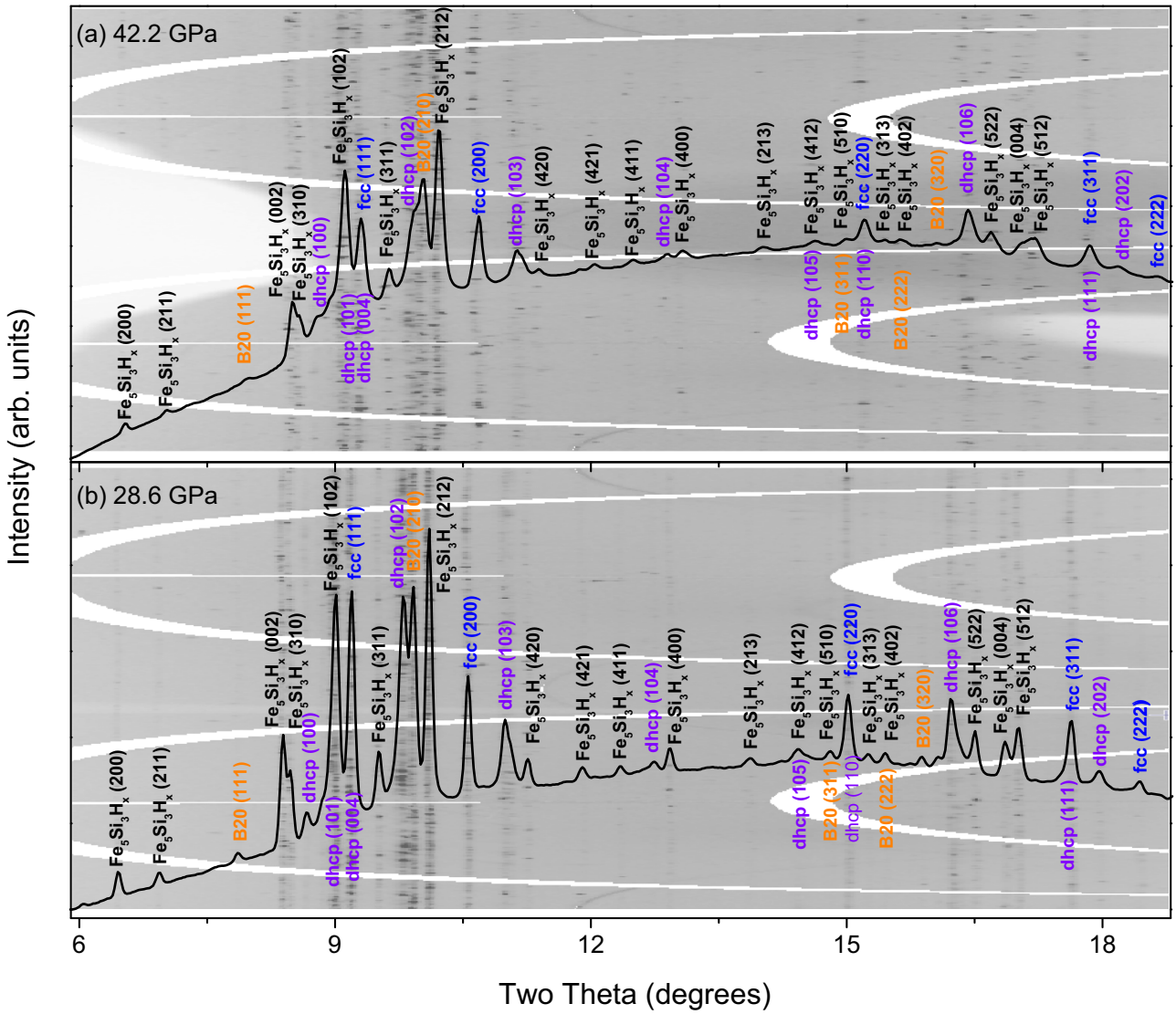

FIG. 3. X-ray diffraction patterns of the synthesized phases from high *P-T* reactions between Fe-9Si alloy and H. (a) 42.2 GPa and (b) 28.6 GPa. The diffraction peaks of $Fe_5Si_3H_x$ (black), fcc FeH_x (blue), dhcp FeH_x (purple), and B20 FeSi (orange) were labeled with their Miller indices. Although some of the diffraction peaks overlap due to the existence of multiple phases, more than 10 diagnostic peaks, that are distinct from any other phases, can be indexed with the hexagonal structure of $Fe_5Si_3H_x$. Diffraction images are plotted as backgrounds. The wavelength of incident x-ray is 0.3344 Å.

interval. A third order Birch-Murnaghan (BM) equation of state (EoS) was used to fit pressure-volume data from DFT calculations as well as experiments.

IV. RESULTS AND DISCUSSION

At 1 bar, it has been debated if the stable crystal structure of Fe-9Si is body-centered cubic (bcc) [20,21,23] or $D0_3$ (BiF_3-type) [22]. Studies suggested that with cold compression conversion of H-free Fe-9Si alloy to a hcp phase starts from ∼16 GPa and completes at ∼36 GPa [21,39,40]. Our XRD patterns show that the unheated Fe-9Si in a H environment completely converts to a hcp structure at 11.0 GPa without additional peaks belonging to bcc or $D0_3$ structures [Fig. 2(a)]. The unheated hcp Fe-9Si exhibits 3–5% greater unit-cell volumes than the H-free Fe-9Si [Fig. 2(c)] (Table S3) [41], suggesting H has been incorporated to form hcp $Fe_{0.83}Si_{0.17}H_x$ by cold compression at 300 K.

An empirical method [47] was used to estimate the hydrogen content (x) in metal alloys based on the volume expansion: $x = (V_{MHx} - V_M)/V_H$, where V_H, V_{MHx}, and V_M are the volume increase per H atom, the volume of metal hydride (MH_x) and the volume of H-free metal (M), respectively. We used an average value of ∼2.5 $Å^3$/(# of metal atoms) for V_H at ambient conditions from previous reports [47,48]. The estimation yields $x \approx 0.28$ in the hcp $Fe_{0.83}Si_{0.17}H_x$, which is smaller than the H content ($x = 0.50$–0.64) reported for the hcp $Fe_{0.88}Si_{0.12}H_x$ alloys [15]. Note that for comparison, we corrected the x value in the hcp $Fe_{0.88}Si_{0.12}H_x$, which was reported as 0.61–0.79 when using a V_H value of ∼2.0 $Å^3$/(# of metal atoms) [15]. In addition, Tagawa *et al.* [15] heated the sample to 1000 K, which may promote H solubility in the $Fe_{0.88}Si_{0.12}$ alloy. Fitting the pressure-volume data of our hcp

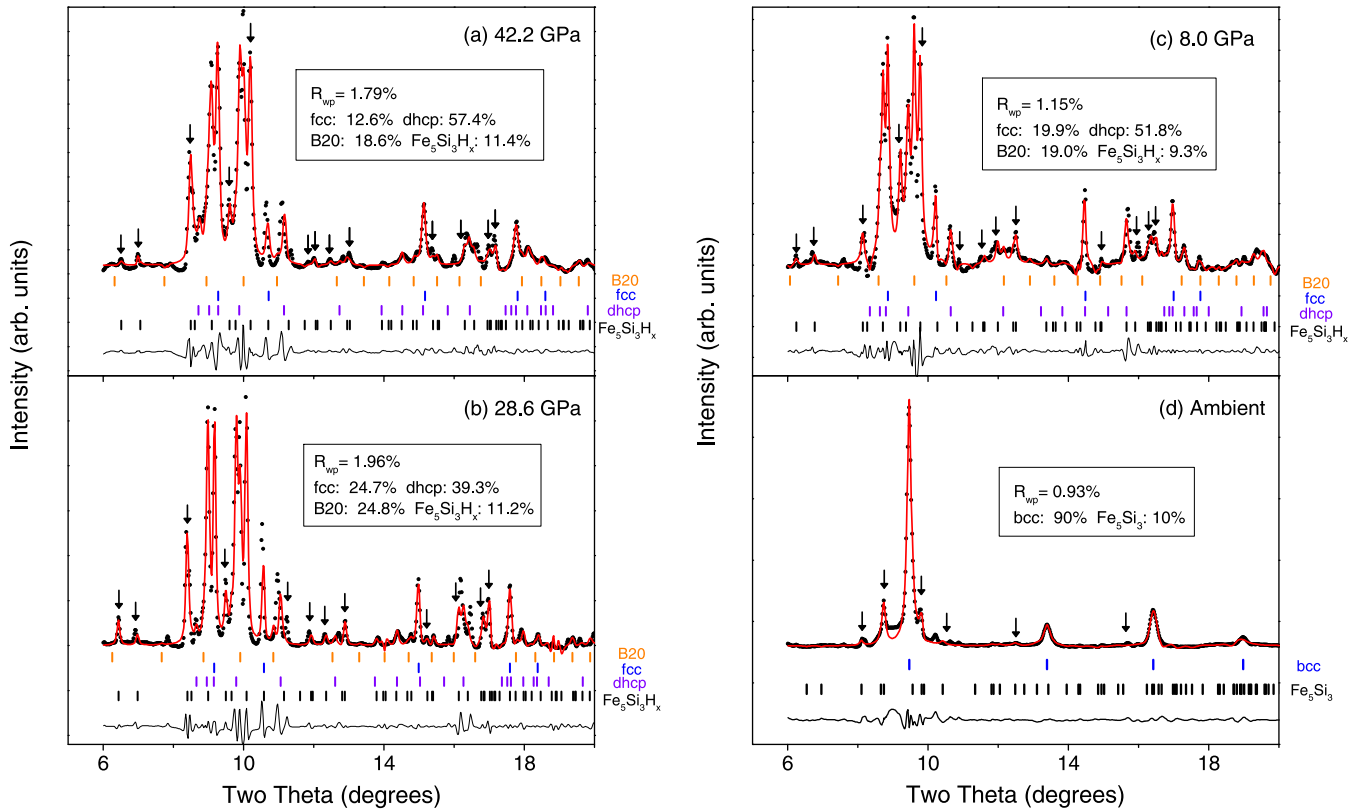

FIG. 4. Rietveld refinements on x-ray diffraction patterns of the synthesized products from Fe-9Si alloys and H. (a) 42.2 GPa. (b) 28.6 GPa. (b) 8.0 GPa. (d) After decompression to ambient conditions. The black circles are experimentally measured intensities, the red lines are the best fits, and the black lines are residuals. Peak positions of different phases are shown in the colored vertical ticks: B20 FeSi (orange), fcc FeH_x (blue), dhcp FeH_x (purple), and $Fe_5Si_3H_x$ (black). The diagnostic peaks that uniquely belong to $Fe_5Si_3H_x$ were labeled out with black arrows on top of them. Fit residue factor (R_{wp}) and mole fractions of phases were provided in the legend. Upon decompression to ambient conditions, FeH_x and $Fe_5Si_3H_x$ phases lose H and convert to bcc Fe and Fe_5Si_3, respectively. The wavelength of incident x-ray is 0.3344 Å.

$Fe_{0.83}Si_{0.17}H_x$ at 300 K yields $V_0 = 12.06(7)$ Å^3/(# of Fe+Si atoms), $K_0 = 162(7)$ GPa, and $K_0' = 4.6(4)$ (Table S4) [19]. Compared with the H-free Fe-9Si (Table S4), the K_0 of H-bearing Fe-9Si changes little but its K_0' decreases by 10–16% even after considering the trade-off in EoS fittings.

Hydrogen-free Fe-16Si has a $D0_3$ structure up to 40 GPa at room temperature [42]. Our XRD patterns show that the unheated Fe-16Si in a H medium maintains a $D0_3$ structure at 12.0–38.2 GPa [Fig. 2(b)] and displays comparable volumes to H-free Fe-16Si [Fig. 2(c)] (Table S3) [42]. This indicates that little or no H enters into the structure of Fe-16Si without heating. Early studies show that pure metallic Fe can react with H to form dhcp FeH_x above 3–4 GPa at room temperature [16,17], while B20 and B2 FeSi do not exhibit such strong hydrogenation behavior with compression at 300 K [27]. Combining the cases of pure Fe metal [16], Fe-6.5Si [15], Fe-9Si, Fe-16Si, and FeSi alloys [27] collectively, we conclude that Si generally reduces the H solubility in Fe-Si alloys at high pressure and 300 K.

We separately laser heated Fe-9Si at 28.6–42.2 GPa and Fe-16Si at ~33.6 GPa in a H medium up to 2000–3000 K. Figures 3–5 and S2 show high-pressure XRD patterns of the reaction products measured after temperature quenched to 300 K during compression and/or decompression. Peak identification and indexing found that both reaction experiments on Fe-9Si and Fe-16Si yield almost identical phases, including B20 FeSi, fcc and dhcp FeH_x, and a hexagonal-structured "Fe_5Si_3"-like phase (space group: $P6_3/mcm$), except for the existence of an additional B2 FeSi in the Fe-16Si run. More than 10 diffraction peaks can be uniquely indexed to the "Fe_5Si_3"-like phase. In our diffraction patterns, the cubic B20 FeSi, B2 FeSi, and fcc FeH_x phases each show more than two diagnostic peaks, and the dhcp FeH_x phase has 4–5 diagnostic peaks. Rietveld refinements with small residual factor ($R_{wp} < 2.4\%$) showed that the "Fe_5Si_3"-like phase makes up approximately 10% of the synthesized products [Figs. 3–5 and S2] (Table S5) [19]. Because of the higher molar mass of the "Fe_5Si_3"-like phase than other phases, it contributes significantly to the diffraction intensities in the measured XRD patterns [Fig. 5]. In addition, the smooth peak position shift trends with decompression as shown in Fig. S3 also support our peak assignments [19].

Comparison of the EoS data of the identified phases with previous experimental reports [Fig. 6] (Table S5) [19] suggests that: (1) The B2 phase has comparable high-pressure volumes to H-free B2 FeSi [39], while the B20 phase shows a slightly higher volume, <1.5%, than H-free B20 FeSi [39]. This observation indicates limited H incorporation in the Si-rich FeSi alloy, which is consistent with recent reports on the low H solubility in FeSi at high P-T [27]; (2) The unit-cell

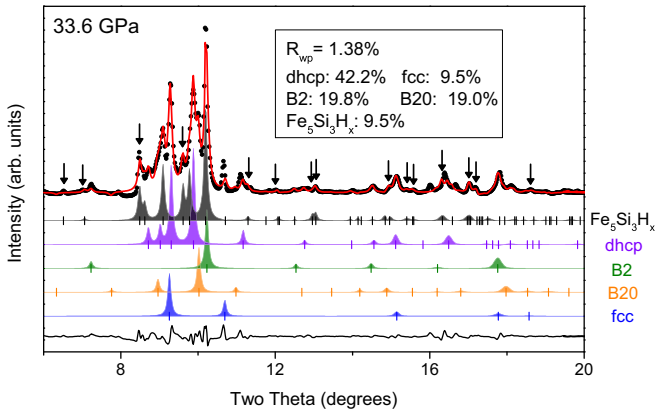

FIG. 5. Rietveld refinements on the XRD pattern of the synthesized products from Fe-16Si alloys and H at 33.6 GPa. The XRD pattern was collected after heating up to 3000 K. The black circles are measured intensities, the red lines are the best fits, and the black lines are fit residuals. Peak positions of B20 FeSi (orange), B2 FeSi (olive), fcc FeH_x (blue), dhcp FeH_x (purple), and $Fe_5Si_3H_x$ (black) were shown as colored ticks. The colored histograms of individual phases were calculated from the Rietveld refinements to show the contributions of different phases to the intensity of the measured pattern. The diagnostic peaks of $Fe_5Si_3H_x$ were indicated with black arrows. Residue factor (R_{wp}) and mole fractions of the phases from the Rietveld refinements were provided in the legend. The wavelength of incident x-ray is 0.3344 Å.

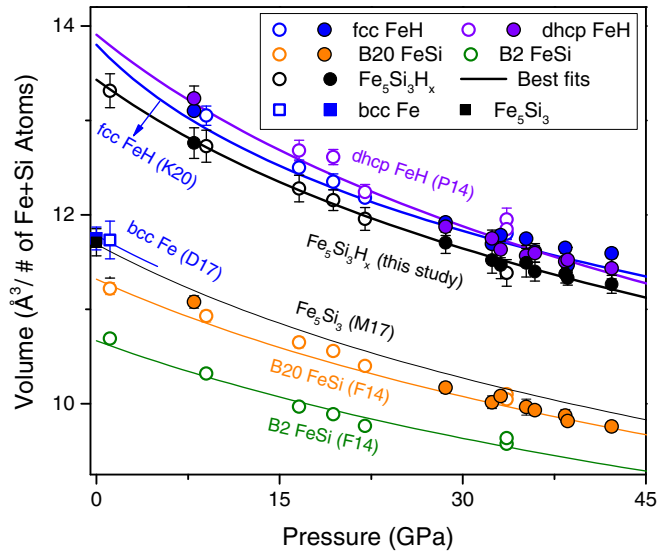

FIG. 6. Pressure-volume relationship of phases synthesized from Fe-Si alloys and H reactions. The measurements were conducted on the reaction products at 300 K during compression and/or decompression. The solid and open symbols are from the runs of Fe-9Si and Fe-16Si, respectively: B2 FeSi (olive circles), B20 FeSi (orange circles), fcc FeH_x (blue circles), dhcp FeH_x (purple circles), and $Fe_5Si_3H_x$ (black circles). The solid black line is the best third order BM EoS fit to the $Fe_5Si_3H_x$ data together from two different runs. Previous experimental reports on B2 FeSi (F14) [39], B20 FeSi (F14) [39], fcc FeH (K20) [43] and dhcp FeH (P14) [17], were plotted as solid lines with corresponding colors for comparison. FeH_x and $Fe_5Si_3H_x$ phases lose H and convert to bcc Fe (blue squares) and Fe_5Si_3 (black squares), respectively, upon recovery to 1 bar. Previous results on bcc Fe (D17) [44] and Fe_5Si_3 (M17) [45] were plotted as blue and black thin lines, respectively. We note that existing EoS data for H-free Fe_5Si_3 [35,45,46] are consistent with each other and here we show data points from McGuire *et al.* [45].

volumes of the fcc and dhcp phases agree well with those of fcc FeH_x and dhcp FeH_x with $x = 1$ [17,43], respectively, indicating that these phases have H/Fe molar ratios close to 1; (3) The unit-cell volume of the hexagonal phase is 12–15% greater than that of H-free Fe_5Si_3 [$\Delta V \approx 1.57 \pm 0.09$ Å^3/ (# of Fe+Si atoms)] [35,45,46]. Since H alloying in Fe metal can typically increase its unit-cell volume [16], we attribute the observed volume expansion to H incorporation into the structure of Fe_5Si_3 to form $Fe_5Si_3H_x$. The observed volume expansion could be used to estimate the H content in $Fe_5Si_3H_x$ by the empirical method [47]. However, validity of the empirical method is not known for ternary hydrogen alloys (in our case Si-rich composition in particular) and the method is developed for binary hydrogen alloys (see later in our DFT approach).

Our experiments on Fe-Si alloys in a H medium were conducted at 28.6–42.2 GPa and the temperature was above 2000 K. McGuire *et al.* [45] show that H-free Fe_5Si_3 is not stable at high temperature and will decompose into cubic FeSi and Fe_3Si above 1300 K at 18 GPa, which is much lower than our experimental *P-T* conditions. This means that the incorporation of H could stabilize the hexagonal phase, and therefore $Fe_5Si_3H_x$. At pressures close to ambient conditions during decompression, dhcp and fcc FeH_x phases recede and bcc Fe appears in the heated spot. This observation indicates that the FeH_x phases lose H with decompression and convert to H-free bcc Fe, consistent with previous experimental observations [16]. The hexagonal phase ($Fe_5Si_3H_x$) maintains an expanded volume to ~1.1 GPa and then exhibits a volume shrink upon quenching to 1 bar. The volume at 1 bar is comparable to that of Fe_5Si_3 [Fig. 6] [45], indicating H escaped during the decompression.

The chemical mappings using EPMA show that the unheated region is chemically homogeneous with compositions consistent with that of the starting material, while the heated spot has a Si-rich rim with a Si-poor center [Figs. 1(c) and 1(f)]. Optical images of the heat regions show an apparent melting signature: removal of much material by the mobility of melt from the heated center toward lower-temperature surroundings [49]. Thus, we believe the liquidus phase exists at the margin, which crystallized first with higher melting temperatures, and the center region should be alloy phases converted from the melt during temperature quench. Quantitative wavelength-dispersive spectroscopy measurements on selected points of the recovered sample show that the Si-rich rim contains about 29 wt % Si, while the center area contains 5.9–7.5 wt % Si (Table S2) [19]. Considering the higher melting temperatures of Fe-Si alloys than that of FeH_x [22,50], the margin area may consist of FeSi (33.3 wt % Si) and $Fe_5Si_3H_x$ (~23.1 wt % Si), and the center region most likely corresponds to the FeH_x alloy observed in XRD. We note that, during decompression to ambient conditions, the sample chamber shrank due to the release of H pressure medium and the sample foil deformed, resulting in different sizes and shapes from that at high pressures [Figs. 1(c)–1(f)].

Therefore, it is difficult to compare details of XRD and EPMA observations beyond first-order distribution of the elements. It is also important to note that the excitation volume in EPMA experiments is larger than the alloy grains of the recovered sample foil, resulting in an averaging effect on measured compositions. On the other hand, XRD does not have the averaging effects and therefore can reveal more details. While transmission electron microscopy (TEM) could provide a better resolution to detect single phases for laser-heated spots in DACs, sample recovery and preparation for TEM analysis were challenging because of the fragile nature of the sample laser heated in a soft H medium at high pressures.

The empirical method [47] to estimate the H content in metals was developed for the close-packed alloys. However, the crystal structure of Fe_5Si_3 is quite different from close-packed structures and therefore the question arises whether the method can be applied to $Fe_5Si_3H_x$. To further gain insights on the amount of H in the hexagonal phase, we conducted DFT calculations (see Sec. III for detailed DFT calculations setup on FM and NM structure models of $Fe_5Si_3H_3$ and Fe_5Si_3). Results on FM and NM Fe_5Si_3 and FM and NM $Fe_5Si_3H_3$ were compared with our experimental data on $Fe_5Si_3H_x$ as well as H-free Fe_5Si_3 [35,45,46].

Our calculated volumes of FM Fe_5Si_3 agree well with previous experimental reports on H-free Fe_5Si_3 within uncertainty (<0.8% difference) at 0–40 GPa [Fig. 7(b)] [45,46]. DFT calculations on NM Fe_5Si_3 predict about 1.8–5.1% smaller volumes than the experimental data of H-free Fe_5Si_3 [45,46]. Earlier Mössbauer study showed a FM ordering for H-free Fe_5Si_3 at 1 bar [36]. Our results also anticipate that Fe_5Si_3 is more likely to be FM at 0–40 GPa. Our measured volumes of the hexagonal $Fe_5Si_3H_x$ show a good agreement (<1.5% difference) with those of both NM and FM $Fe_5Si_3H_3$ from DFT calculations, considering the experimental uncertainties [Fig. 7(b)]. Fitting the experimental pressure-volume data of $Fe_5Si_3H_x$ to third order BM EoS yields $V_0 = 13.43(9)$ Å^3/(# of Fe+Si Atoms), $K_0 = 147(12)$ GPa, and $K_0' = 5.1(6)$. In comparison, we obtained $K_0 = 155.6$ GPa and $K_0' = 4.1$ ($V_0 = 13.5$ Å^3/(# of Fe+Si atoms), fixed) for FM $Fe_5Si_3H_3$, and $K_0 = 169.1$ GPa and $K_0' = 4.5$ ($V_0 = 13.1$ Å^3/(# of Fe+Si atoms), fixed) for NM $Fe_5Si_3H_3$, respectively (Table S4) [19]. Taking into account the trade-off in BM EoS fittings and experimental uncertainties, the K_0 of synthesized $Fe_5Si_3H_x$ is comparable with those of both FM and NM phases, while its K_0' is higher. Compared to H-free Fe_5Si_3 (Table S4) [35,45,46], the V_0 of our experimental $Fe_5Si_3H_x$ is about 14.7% higher, while its K_0 decreases and K_0' increases, indicating a strong H incorporation effect on the EoS parameters of Fe-Si alloys. We should note that the DFT was conducted for static lattice conditions, while experimental measurements were performed at 300 K.

The DFT calculations predict that FM $Fe_5Si_3H_3$ has 2.1–3.1% higher volumes than the NM case at 0–40 GPa. The volume expansion caused by magnetic ordering is much smaller than that by H incorporation, suggesting that our observed volume expansion in Fe_5Si_3 should mainly result from the H solubility. Although we do not have direct experimental chemical or neutron diffraction measurements on the H content in the synthesized phase in this study, to first order, the great agreement on the volumes between DFT and experimental data supports the synthesis of the new ternary alloy $Fe_5Si_3H_x$. More detailed information on other properties of FM and NM $Fe_5Si_3H_3$ is provided in the Supplemental Material drawn from our DFT calculations [19] (see also Refs. [51,52] therein). While we believe that the level of agreement is adequate to explain the experimentally observed volume expansion, future detailed DFT investigation is still

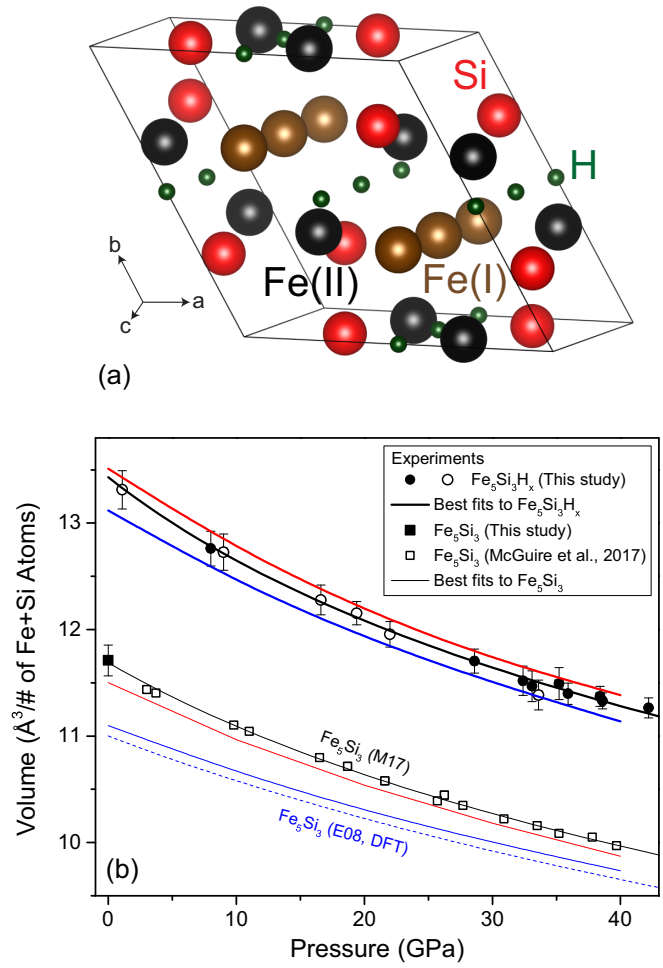

FIG. 7. Density functional theory calculations on $Fe_5Si_3H_3$ and Fe_5Si_3 at high pressure. (a) A crystal structure model of $Fe_5Si_3H_3$ ($Z = 22$) at 0 GPa from the DFT calculations. The crystal structure of $Fe_5Si_3H_3$ is modified from that of Fe_5Si_3 [35] by placing H atoms at (0.5, 0.5, 0.5), (0.5, 0, 0.5), and (0.5, 0, 0). (b) Pressure-volume relationship. Thick and thin lines are for $Fe_5Si_3H_3$ and Fe_5Si_3, respectively, and red and blue colors are used for ferromagnetic and nonmagnetic calculations, respectively. Solid and open circles are our experimental data points of the synthesized $Fe_5Si_3H_x$ from the runs of Fe-9Si and Fe-16Si, respectively. The solid black squares are from the recovered sample at ambient conditions. Open black squares are for H-free Fe_5Si_3 from McGuire *et al.* [45]. Thick and thin black lines are the best third order BM EoS fits to $Fe_5Si_3H_x$ in this study and Fe_5Si_3 by McGuire *et al.* [45], respectively. The dashed blue line is from an earlier DFT calculation on H-free Fe_5Si_3 [46] for comparison.

required to decipher the structure, composition, and magnetic ordering of the new $Fe_5Si_3H_x$ ternary phase.

V. CONCLUSIONS

We found the appearance of a hexagonal-structured Fe-Si-H ternary phase, $Fe_5Si_3H_x$, at high pressures after heating up to 3000 K, which was observed for the first time to our knowledge. Comparison between the observed volume expansion and DFT calculations suggests the H/Fe ratio is about 0.6 in this phase. This is in contrast with Si-rich B20 and B2 FeSi alloys with little H solubility [27]. It is important to note that Fe_5Si_3 is not stable above 1300 K at 18 GPa [45] and therefore H plays an important role for the high P-T stability.

Our high-pressure experiments also showed that Fe-9Si and Fe-16Si break down in a H medium upon laser heating up to 3000 K at 28.6–42.2 GPa. The reaction produces Fe-rich (dhcp and fcc FeH_x), Si-rich (B20 and B2 FeSi) and a Fe-Si-H ternary phase. In our experiments, the sample was heated above the melting temperatures of Fe–Si–H. The texture and chemical measurements show that Si-rich alloys are likely formed as solidus phases and H-rich alloys are from the quenched melt. Such an observation can have important implications for the crystallization at the solid-liquid boundary of planetary cores, such as the Earth's inner and outer core boundary. In the Earth's inner core, significant heterogeneities have been documented in seismic studies [53], which could be a record of a time-dependent crystallization pattern at the solid-to-liquid core boundary. The role of light elements on the crystallization process of Fe-rich metal is important to understand the compositional effect on dynamo generation [54]. Although our study did not reach the pressure of Earth's core, the experimental conditions here are relevant to the cores of Mars or Mars-sized exoplanets [55]. Recently the InSight mission revealed that the Martian core is much larger than previously believed, and thus, should have a low density and large concentrations of light elements [56]. Furthermore, geodetic measurements have shown that the significant part of the Martian core is in a liquid state [57]. Therefore, the phase relations found in this study will be important for understanding the metallic cores of such smaller planets and their magnetic history.

ACKNOWLEDGMENTS

The authors acknowledge J. Yang in the Carnegie Institution for Science for providing the starting Fe-9Si alloy, which was commercially bought from GoodFellow Corporation. The authors thank A. Wittmann for his assistance on electron microprobe experiments. This work is supported by NSF-Astronomical Science (AST200567) and NSF-Earth Science (EAR1921298). We acknowledge the support of GeoSoilEnviroCARS (University of Chicago, Sector 13) for synchrotron experiments. GeoSoilEnviroCARS was supported by the National Science Foundation - Earth Sciences (EAR-1634415). This research used resources of the Advanced Photon Source, a U.S. Department of Energy (DOE) Office of Science User Facility operated for the DOE Office of Science by Argonne National Laboratory under Contract No. DE-AC02-06CH11357.

[1] J. M. Day, D. G. Pearson, and L. A. Taylor, Highly siderophile element constraints on accretion and differentiation of the earth-moon system, Science **315**, 217 (2007).

[2] R. J. Walker, Highly siderophile elements in the earth, moon and mars: Update and implications for planetary accretion and differentiation, Geochemistry **69**, 101 (2009).

[3] K. Hirose, S. Labrosse, and J. Hernlund, Composition and state of the core, Annu. Rev. Earth Planet. Sci. **41**, 657 (2013).

[4] J. Li and Y. Fei, Experimental constraints on core composition, in *Treatise on Geochemistry*, edited by K. Turekian and H. Holland (Elsevier, Amsterdam, 2003), Vol. 2, p. 568.

[5] V. Clesi, M. A. Bouhifd, N. Bolfan-Casanova, G. Manthilake, F. Schiavi, C. Raepsaet, H. Bureau, H. Khodja, and D. Andrault, Low hydrogen contents in the cores of terrestrial planets, Sci. Adv. **4**, e1701876 (2018).

[6] R. Iizuka-Oku, T. Yagi, H. Gotou, T. Okuchi, T. Hattori, and A. Sano-Furukawa, Hydrogenation of iron in the early stage of earth's evolution, Nat. Commun. **8**, 14096 (2017).

[7] T. Okuchi, Hydrogen partitioning into molten iron at high pressure: Implications for earth's core, Science **278**, 1781 (1997).

[8] S. Tagawa, N. Sakamoto, K. Hirose, S. Yokoo, J. Hernlund, Y. Ohishi, and H. Yurimoto, Experimental evidence for hydrogen incorporation into earth's core, Nat. Commun. **12**, 2588 (2021).

[9] Y. Li, L. Vočadlo, T. Sun, and J. P. Brodholt, The earth's core as a reservoir of water, Nat. Geosci. **13**, 453 (2020).

[10] M. Kilburn and B. Wood, Metal-silicate partitioning and the incompatibility of S and Si during core formation, Earth Planet. Sci. Lett. **152**, 139 (1997).

[11] A. Ricolleau, Y. Fei, A. Corgne, J. Siebert, and J. Badro, Oxygen and silicon contents of earth's core from high pressure metal–silicate partitioning experiments, Earth Planet. Sci. Lett. **310**, 409 (2011).

[12] S. Cui and I.-H. Jung, Critical reassessment of the Fe-Si system, Calphad **56**, 108 (2017).

[13] H. Yamane and T. Yamada, Effects of stacking fault on the diffraction intensities of β-fesi2, J. Alloys Compd. **476**, 282 (2009).

[14] O. Kubaschewski, *Iron-Binary Phase Diagrams* (Springer Science & Business Media, New York, 2013).

[15] S. Tagawa, K. Ohta, K. Hirose, C. Kato, and Y. Ohishi, Compression of Fe–Si–H alloys to core pressures, Geophys. Res. Lett. **43**, 3686 (2016).

[16] J. Badding, R. Hemley, and H. Mao, High-pressure chemistry of hydrogen in metals: *In situ* study of iron hydride, Science **253**, 421 (1991).

[17] C. M. Pépin, A. Dewaele, G. Geneste, P. Loubeyre, and M. Mezouar, New Iron Hydrides Under High Pressure, Phys. Rev. Lett. **113**, 265504 (2014).

[18] C. Pépin, G. Geneste, A. Dewaele, M. Mezouar, and P. Loubeyre, Synthesis of FeH_5: A layered structure with atomic hydrogen slabs, Science **357**, 382 (2017).

[19] See Supplemental Material at http://link.aps.org/supplemental/10.1103/PhysRevB.105.104111 for experimental raw data and figures as well as additional DFT calculation results showing robustness of our phase identification.

[20] H. Huang, C. Leng, Q. Wang, G. Young, X. Liu, Y. Wu, F. Xu, and Y. Fei, Equation of state for shocked Fe-8.6 wt % Si up to 240 GPa and 4670 K, J. Geophys. Res.: Solid Earth **124**, 8300 (2019).

[21] N. Hirao, E. Ohtani, T. Kondo, and T. Kikegawa, Equation of state of iron-silicon alloys to megabar pressure, Phys. Chem. Miner. **31**, 329 (2004).

[22] R. A. Fischer, A. J. Campbell, D. M. Reaman, N. A. Miller, D. L. Heinz, P. Dera, and V. B. Prakapenka, Phase relations in the Fe–FeSi system at high pressures and temperatures, Earth Planet. Sci. Lett. **373**, 54 (2013).

[23] J. Zhang and F. Guyot, Thermal equation of state of iron and $Fe_{0.91}$ $Si_{0.09}$, Phys. Chem. Miner. **26**, 206 (1999).

[24] Y. Ye, S.-H. Shim, V. Prakapenka, and Y. Meng, Equation of state of solid Ne inter-calibrated with the MgO, Au, Pt, NaCl-B2, and ruby pressure scales up to 130 GPa, High Pressure Res. **38**, 377 (2018).

[25] A. F. Goncharov, V. B. Prakapenka, V. V. Struzhkin, I. Kantor, M. L. Rivers, and D. A. Dalton, X-ray diffraction in the pulsed laser heated diamond anvil cell, Rev. Sci. Instrum. **81**, 113902 (2010).

[26] G. Zhang, H. Yukawa, N. Watanabe, Y. Saito, H. Fukaya, M. Morinaga, T. Nambu, and Y. Matsumoto, Analysis of hydrogen diffusion coefficient during hydrogen permeation through pure niobium, Int. J. Hydrogen Energy **33**, 4419 (2008).

[27] S. Fu, S. Chariton, V. B. Prakapenka, A. Chizmeshya, and S.-H. Shim, Hydrogen solubility in fesi alloy phases at high pressures and temperatures, Am. Mineral., doi:10.2138/am-2022-8295.

[28] S.-H. Shim, PeakPo–A python software for x-ray diffraction analysis at high pressure and high temperature, Zenodo (2020), doi:10.5281/zenodo.3726423.

[29] B. H. Toby and R. B. Von Dreele, GSAS-II: The genesis of a modern open-source all purpose crystallography software package, J. Appl. Cryst. **46**, 544 (2013).

[30] P. E. Blöchl, Projector augmented-wave method, Phys. Rev. B **50**, 17953 (1994).

[31] J. J. Mortensen, L. B. Hansen, and K. W. Jacobsen, Real-space grid implementation of the projector augmented wave method, Phys. Rev. B **71**, 035109 (2005).

[32] J. P. Perdew, K. Burke, and M. Ernzerhof, Generalized Gradient Approximation Made Simple, Phys. Rev. Lett. **77**, 3865 (1996).

[33] R. Caracas and R. Wentzcovitch, Equation of state and elasticity of FeSi, Geophys. Res. Lett. **31**, L20603 (2004).

[34] T. Tsumuraya, Y. Matsuura, T. Shishidou, and T. Oguchi, First-principles study on the structural and magnetic properties of iron hydride, J. Phys. Soc. Jpn. **81**, 064707 (2012).

[35] D. Santamarıa-Pérez, J. Nuss, J. Haines, M. Jansen, and A. Vegas, Iron silicides and their corresponding oxides: A high pressure study of Fe_5Si_3, Solid State Sci. **6**, 673 (2004).

[36] C. Johnson, J. Forsyth, G. Lander, and P. Brown, Magnetic moments and hyperfine interactions in carbon-stabilized Fe_5 Si_3, J. Appl. Phys. **39**, 465 (1968).

[37] G. Rollmann, P. Entel, A. Rohrbach, and J. Hafner, High-pressure characteristics of α-Fe_2O_3 using DFT + U, Phase Trans. **78**, 251 (2005).

[38] Y. S. Mohammed, Y. Yan, H. Wang, K. Li, and X. Du, Stability of ferromagnetism in Fe, co, and ni metals under high pressure with GGA and GGA + U, J. Magn. Magn. Mater. **322**, 653 (2010).

[39] R. A. Fischer, A. J. Campbell, R. Caracas, D. M. Reaman, D. L. Heinz, P. Dera, and V. B. Prakapenka, Equations of state in the Fe-Fesi system at high pressures and temperatures, J. Geophys. Res.: Solid Earth **119**, 2810 (2014).

[40] J.-F. Lin, A. J. Campbell, D. L. Heinz, and G. Shen, Static compression of iron-silicon alloys: Implications for silicon in the earth's core, J. Geophys. Res.: Solid Earth **108**, 2045 (2003).

[41] S. Tateno, Y. Kuwayama, K. Hirose, and Y. Ohishi, The structure of Fe–Si alloy in earth's inner core, Earth Planet. Sci. Lett. **418**, 11 (2015).

[42] R. A. Fischer, A. J. Campbell, R. Caracas, D. M. Reaman, P. Dera, and V. B. Prakapenka, Equation of state and phase diagram of Fe–16Si alloy as a candidate component of earth's core, Earth Planet. Sci. Lett. **357**, 268 (2012).

[43] C. Kato, K. Umemoto, K. Ohta, S. Tagawa, K. Hirose, and Y. Ohishi, Stability of fcc phase Feh to 137 GPa, Am. Mineral. **105**, 917 (2020).

[44] P. I. Dorogokupets, A. M. Dymshits, K. D. Litasov, and T. S. Sokolova, Thermodynamics and equations of state of iron to 350 GPa and 6000 K, Sci. Rep. **7**, 41863 (2017).

[45] C. McGuire, D. Santamaria-Pérez, A. Makhluf, and A. Kavner, Isothermal equation of state and phase stability of Fe_5Si_3 up to 96 GPa and 3000 k, J. Geophys. Res.: Solid Earth **122**, 4328 (2017).

[46] D. Errandonea, D. Santamaria-Perez, A. Vegas, J. Nuss, M. Jansen, P. Rodríguez-Hernandez, and A. Muñoz, Structural stability of Fe_5 Si_3 and Ni_2 Si studied by high-pressure x-ray diffraction and *ab initio* total-energy calculations, Phys. Rev. B **77**, 094113 (2008).

[47] Y. Fukai, Some properties of the Fe-H system at high pressures and temperatures, and their implications for the earth's core, in *High Pressure Research: Application to Earth and Planetary Sciences* (TERRAPUB, Tokyo, 1992).

[48] A. Machida, H. Saitoh, H. Sugimoto, T. Hattori, A. Sano-Furukawa, N. Endo, Y. Katayama, R. Iizuka, T. Sato, M. Matsuo, S. Orimo, and K. Aoki, Site occupancy of interstitial deuterium atoms in face-centered-cubic iron, Nat. Commun. **5**, 5063 (2014).

[49] D. Andrault, S. Petitgirard, G. L. Nigro, J.-L. Devidal, G. Veronesi, G. Garbarino, and M. Mezouar, Solid–liquid iron partitioning in earth's deep mantle, Nature (London) **487**, 354 (2012).

[50] K. Hirose, S. Tagawa, Y. Kuwayama, R. Sinmyo, G. Morard, Y. Ohishi, and H. Genda, Hydrogen limits carbon in liquid iron, Geophys. Res. Lett. **46**, 5190 (2019).

[51] H. Mao, Y. Wu, L. Chen, J. Shu, and A. P. Jephcoat, Static compression of iron to 300 GPa and $Fe_{0.8}Ni_{0.2}$ alloy to 260 GPa: Implications for composition of the core, J. Geophys. Res.: Solid Earth **95**, 21737 (1990).

[52] A. K. Singh, C. Balasingh, H.-K. Mao, R. J. Hemley, and J. Shu, Analysis of lattice strains measured under nonhydrostatic pressure, J. Appl. Phys. **83**, 7567 (1998).

[53] A. Deuss, Heterogeneity and anisotropy of earth's inner core, Annu. Rev. Earth Planet. Sci. **42**, 103 (2014).

[54] B. A. Buffett, H. E. Huppert, J. R. Lister, and A. W. Woods, On the thermal evolution of the Earth's core, J. Geophys. Res. **101**, 7989 (1996).

[55] D. Jontof-Hutter, J. F. Rowe, J. J. Lissauer, D. C. Fabrycky, and E. B. Ford, The mass of the mars-sized exoplanet kepler-138 b from transit timing, Nature (London) **522**, 321 (2015).

[56] S. C. Stähler, A. Khan, W. B. Banerdt, P. Lognonné, D. Giardini, S. Ceylan, M. Drilleau, A. C. Duran, R. F. Garcia, Q. Huang *et al.*, Seismic detection of the martian core, Science **373**, 443 (2021).

[57] C. Yoder, A. Konopliv, D. Yuan, E. Standish, and W. Folkner, Fluid core size of Mars from detection of the solar tide, Science **300**, 299 (2003).